Spectral Characteristics of Hot Electron Electroluminescence in Silicon Avalanching Junctions

Monuko du Plessis, *Senior Member, IEEE,* Petrus Johannes Venter, *Senior Member, IEEE,* and Enrico Bellotti, *Associate Member, IEEE*

***Abstract*— The emission spectra of avalanching n^+p junctions manufactured in a standard 350-nm CMOS technology with no process modifications are measured over a broad spectral range and at different current levels. In contrast to the narrow-band forward-biased pn junction emission spectrum, the reverse biased avalanching emission spectrum extends from the ultraviolet 350 nm (3.6 eV) to the near infrared 1.7 μm (0.7 eV), covering the visual range. The photon emission energy spectrum is compared to the hot electron energy distribution within the conduction band, as determined from a full band Monte Carlo simulation. This allows the identification of phonon assisted indirect intraband (*c-c*) hot electron transitions as the dominant physical light emission processes within the high electric field avalanching junction. Device simulations are utilized to identify the device drift region as the source of the near infrared emissions.**

***Index Terms*— Avalanche, electroluminescence, photon emission, spectrum.**

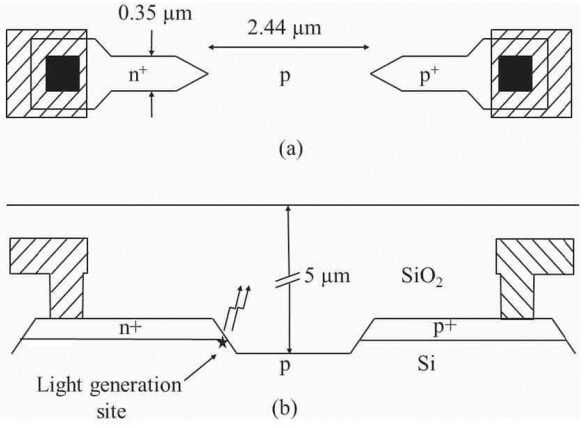

Fig. 1. (a) Layout design of CMOS n^+p point source, and (b) cross section of n^+p point source. Light generation takes place along the sidewall of the LOCOS (local oxidation) structure.

I. Introduction

THE quest for an efficient light source in silicon has been described in the past as looking for the Holy Grail of the silicon integrated circuit technology [1]. This quest is still ongoing and several approaches are followed to generate photons in the indirect band gap silicon material. These techniques include [2] dislocation-based silicon after boron implantation, silicon nanocrystals embedded in oxide, porous silicon structures, Er doping of silicon, Si/Ge quantum dots and ion implanted Si in SiO_2. The possibility of realizing a silicon laser has been proposed previously [1]. Since then significant progress has been made towards this aim using a variety of approaches (e.g. an optically pumped Raman silicon-based laser) for creating lasers on silicon [3]. A very interesting approach was to combine silicon nanocrystals incorporated in a silica matrix with Er^{3+} doping to generate light emission around 1500 nm in silicon, since Er-doped Si-ncs behave as electron-hole pair traps [4].

M. du Plessis and P. J. Venter are with the Carl and Emily Fuchs Institute for Microelectronics, Department of Electrical, Electronic and Computer Engineering, University of Pretoria, Pretoria 0002, South Africa (e-mail: monuko@up.ac.za; jannes.venter@up.ac.za).

E. Bellotti is with the Electrical and Computer Engineering Department, Boston University, Boston, MA 02215 USA (e-mail: bellotti@bu.edu).

However, the key to successful commercialization of any silicon-based light source technology will be to develop a high-volume manufacturing process where light sources can be processed in a CMOS fabrication facility alongside existing CMOS wafers in order to amortize their costs [5]. CMOS compatibility is of the utmost performance in order to take advantage of the vast investment in current CMOS fabrication facilities. All of the above-mentioned technological approaches to manufacture silicon-based light sources necessitate modifications to existing CMOS processes.

Our approach is quite different, namely investigating the silicon light source devices already present in state-of-the-art CMOS technologies, thus eliminating the CMOS compatible issue completely since our devices are 100 % CMOS with no process modifications [6]. Specifically, we are investigating the electroluminescence of hot electrons under high electric field conditions. CMOS based light sources may find a wide range of applications if adequate levels of internal quantum efficiency and external power efficiency can be reached. Applications already proposed and demonstrated include micro displays [7], [8] short haul optical data links [9], [10] and lab-on-chip systems [11], [12]. Although the phenomenon of light emission from a silicon avalanching junction has been known for more than 57 years [13], the physical light generation mechanisms have been studied in more detail only

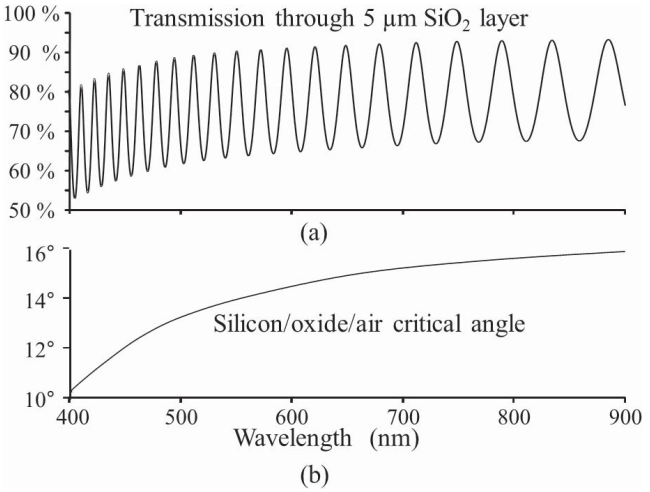

Fig. 2. (a) Calculated transmission of radiation through the 5 μm thick silicon dioxide layer, and (b) the calculated critical angle for total internal reflection in the silicon.

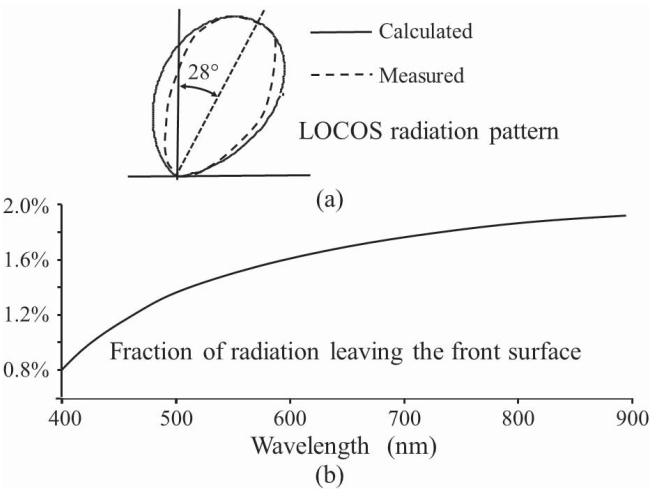

Fig. 3. (a) Measured and calculated radiation pattern, and (b) the fraction of total light being generated that will leave the front surface of the device.

during the last two decades. Even today, the dominant physical mechanisms responsible for photon generation in avalanching indirect band gap semiconductor junctions are not well known and/or generally accepted. In this paper we will use wideband spectral measurements, combined with Monte Carlo device simulations and one dimensional device simulations to identify the dominant radiative processes.

II. Methodology

A. Device Design

The pn junctions under investigation were designed and manufactured in the standard *ams* 0.35 µm CMOS foundry process without any post-processing. The n^+ to p-substrate junction was chosen as the junction of interest, and the layout was performed with the aim to achieve as high an electric field as possible, as will be discussed later. The layout and cross section of a single point source test device are shown in Fig. 1. The n^+ in p-substrate junction forms a sharp tip, pointing towards a p^+ substrate contact, to increase both the electric field and current density when avalanching takes place. Care was taken with the layout to prevent light being reflected from or shielded by any metal layers in close proximity. To achieve higher levels of optical power being emitted, 400 identical point sources were connected in parallel to form an array. The nominal test current was 140 mA, with 350 µA flowing in each point source at 10.5 V reverse bias. An important design consideration when designing pn junctions in avalanche breakdown is the current density in the device. At 140 mA, and with the junction depth of 0.2 µm, the maximum current density in the pn junction is determined as 500 kA/cm^2. This sounds quite high, but when compared to the current densities in the NMOS transistors, it is still within limits. The maximum saturated "on drive current" density measured in the NMOS transistors with 3.3 V bias on gate and drain is 600 µA/µm width as specified by the manufacturing foundry, which corresponds to a maximum "on" drain current of 210 µA/0.35 µm width. This shows that the maximum reverse bias current of 350 µA per point source is only 67 % higher than that experienced in the NMOS transistor drain/source region under normal operating conditions.

B. Spectral Measurements

The output spectra of the array of 400 point sources were measured using two different spectrometers, namely 1) a Si UV-Vis-NIR spectrometer (Avantes AvaSpec 2048TEC) covering the range 250 nm to 1100 nm, and 2) an InGaAs NIR spectrometer (B&WTEK SOL 1.7) covering the wavelength range 900 nm to 1700 nm. From the known relative responses of the two spectrometers, as well as their overlapping spectral ranges, the two spectra could be merged into one externally observed spectrum. From these measured spectra, as well optical power measurements from an International Light Radiometer (IL1700) power meter using a silicon detector SED100 covering the range 250 nm to 1100 nm, and a InGaAs detector SED007 covering the range 800 nm tot 1600 nm, the photon emission rates at the light generation site within the silicon bulk could be determined. Aspects to consider were the transmission through the thick oxide layer, as well as the effect of the critical angle for total internal reflection within the silicon. The calculated spectral characteristics of the oxide transmission and the silicon critical angle are illustrated in Fig. 2.

In Fig. 2 the effect of the increase of the silicon refractive index at shorter wavelengths can be seen. Also very evident is the interference patterns of transmission through a relatively thick oxide layer. It is important to note that a smaller critical angle at shorter wavelengths will lead to less radiation leaving the front surface of the device. Fig. 3 shows the calculated and measured radiation pattern, as well as the fraction of light leaving the front surface as a function of wavelength.

The measured radiation pattern was slightly narrower than the calculated one, and the peak radiation at an angle of 28° from the vertical corresponds to a 45° angle of the LOCOS sidewall. Taking all of the effects into account it follows from Fig. 3(b) that at 400 nm only 0.8 % of the generated light will leave the front surface. This value increases to about 2 % at

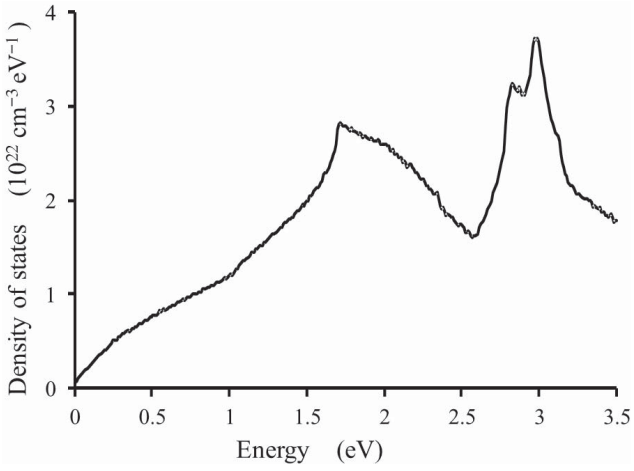

Fig. 4. Monte Carlo simulated density of states (DOS) function derived from the silicon band structure, showing two peaks near 1.7 eV and 2.9 eV.

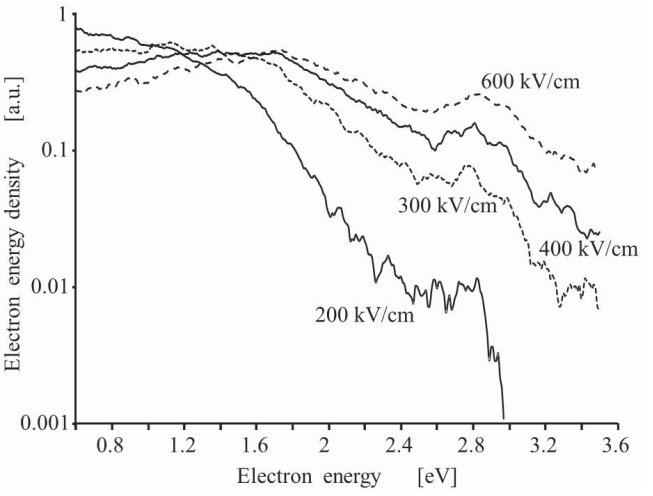

Fig. 5. Electron energy density EED as a function of electric field. The high energy electron density values increases rapidly with increasing electric field. The second maximum in the DOS function at energy of 2.9 eV also becomes apparent at high electric fields.

longer wavelengths. With these simulation results the relative spectrum of the generated light within the silicon could be determined.

C. Monte Carlo Simulations

Key characteristics of our full band Monte Carlo (FBMC) model are the material electronic structure and the carrier phonon scattering rates [14]. The electronic structure is obtained by means of a nonlocal empirical pseudo potential method and the phonon-carrier scattering rates are determined from Fermi's golden rule, accounting for the band structure and the lattice dynamics. This model is material-independent, and provides great flexibility in the ability to characterize many different semiconductor materials. This fully numerical model leads to reliable transport-related results for bulk material, as well as for device structures. The density of states (DOS) for both valence and conduction bands is computed before analyzing the carrier transport properties. The first Brillouin zone is discretized in a number of cubes in k-space and the energy at each corner is evaluated. These values are subsequently used to interpolate the energy values at any arbitrary k-points within each cube. The DOS is computed using a dense mesh of k-points within each cube and for each of this point the energy values are binned and the number of states per-bin is used to obtain the total DOS for each band.

The electron distribution function is computed for a given electric field strength using the following approach. An ensemble of 40 000 particles (either electrons or holes) is simulated for a period of 5 ps. During this period of time, the statistics of a number of variables, namely velocity, energy and position, are collected. At the end of the Monte-Carlo run the statistic on the energy distribution is used to compute the electron number distribution function and the non-equilibrium probability density function. We perform this calculation for a number of electric filed strengths between 200 kV/cm and 600 kV/cm.

In Fig. 4 is shown the Monte Carlo simulation of the DOS (density of states) function for the silicon band structure. The first maximum near 1.7 eV and the second maximum near 2.9 eV are known characteristics of the DOS function [15], [16].

III. Hot Electron Energy Distribution

In an avalanching pn junction depletion region the electric field is relatively high and electrons drifting through the depletion region will be excited to higher energies. These hot electrons will generate additional electron/hole pairs through impact ionization. It is important to know the EED (electron energy distribution) function within the conduction band as a function of electric field. The EED function can be derived from the DOS function and the probability distribution function of electrons.

Monte Carlo simulations were performed at four values of electric field, namely at 200, 300, 400 and 600 kV/cm. The simulation results are shown in Fig. 5. These results correlate well with other high electric field hot electron energy distributions [15], [17].

The main features from Fig. 5 are;

1) A broad spectral peak centered around 1.6 eV and a second, more narrow peak near 2.9 eV. These peaks are due to the DOS function shown in Fig. 2.
2) The energy density of electrons at lower energy levels increases with a decrease in electric field.
3) The energy density of electrons at higher energy levels increases with an increase in electric field.
4) The broad peak around 1.6 eV shifts to lower energies when the electric field is reduced.

From the EED graphs in Fig. 5 it can be reasoned that if the photon generation rate within the pn junction depletion region scales with the electron energy density, then the photon generation as a result of the electrons at an electron energy level of 2.9 eV will be quite small, especially at lower electric fields. In order to experimentally observe the photons being generated by the 2.9 eV hot electrons, the electric field should be quite high and in excess of 400 kV/cm. Earlier efforts to measure

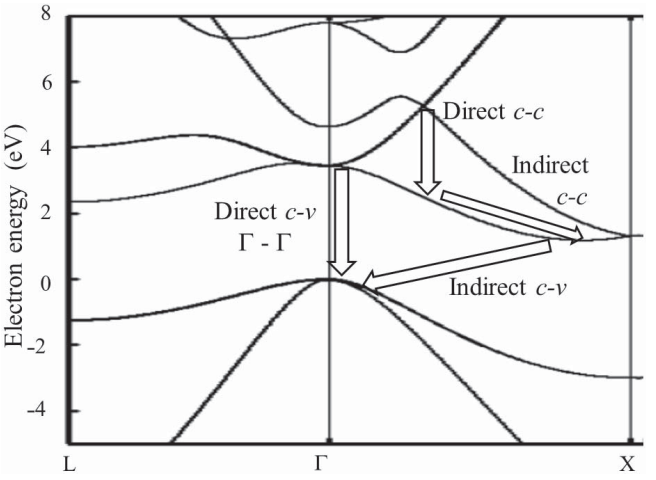

Fig. 6. The four radiative processes in our devices to be considered, namely direct and indirect interband (*c-v*) recombination, and direct and indirect intraband hot electron (*c-c*) transitions.

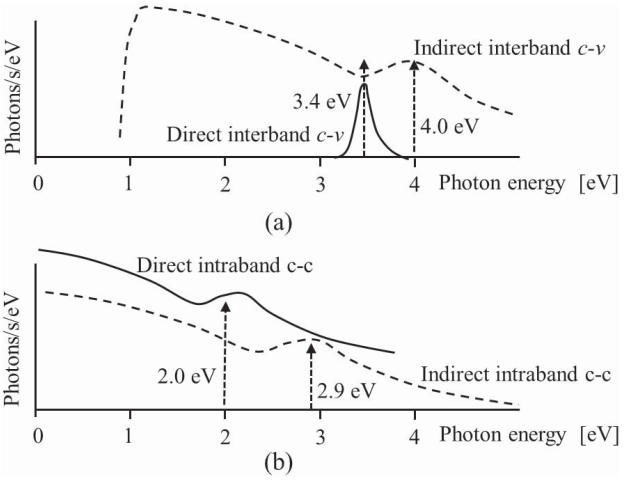

Fig. 7. Expected photon emission spectra for a) direct and indirect interband *c-v* recombination of electrons and holes, and b) direct and indirect intraband *c-v* hot electron transitions under high electric field conditions. Indirect processes are shown as dashed lines and the direct processes as solid lines.

the avalanche electroluminescent emission spectrum almost always resulted in a very smooth, continuously decreasing emission spectrum without any observable peaks, except for some silicon-oxide-air interference patterns. We ascribe this to not enough carriers at high electric fields in those devices [18], [19]. It also follows from this that without the presence of a "signature" energy peak in the emission spectrum almost any theoretical photon generation method could be fitted to the smoothly decreasing emission spectrum. In fact, three separate mechanisms could easily be fitted to the emission spectrum with no discernable transition region from one mechanism to another [20].

IV. Photon Generation Theories

A. Early Observations

One of the very first reports on the phenomenon of avalanche electroluminescence observed a smooth photon emission spectrum [18], continuously decreasing from a photon energy of 1.0 eV to 3.15 eV. It was postulated that the high photon energy light generation was due to indirect radiative conduction to valence interband (*c-v*) recombination between either 1) energetic (hot) electrons with holes in equilibrium with the lattice, or 2) hot holes with electrons in equilibrium with the lattice, or 3) hot electrons with hot holes. The ionization energy of electrons and holes was assumed to be 2.3 eV, and that meant that the photon energy emitted should vary from a 1.1 eV minimum to a maximum photon energy of 3.4 eV. This maximum was in agreement with the observation. Significant near infrared photon emission below 1.1 eV photon energy was also observed [18]. This was attributed to radiative intraband transitions by either energetic electrons (*c-c* transitions) or energetic holes (*v-v* transitions). It was reasoned that for such intraband transitions, there should not be a lower energy limit, but a maximum energy limit of about 2.3 eV. This was a first attempt to describe avalanche photon emission by two mechanisms, although the emission spectrum was a smooth deceasing function with no apparent transition region where one mechanism became more dominant than the other. Four years later [21] it was postulated that the low energy photons might be a result of dominant intra valence band transitions (*c-c*) of hot holes.

Subsequent work [22] with devices where a high electric field could be obtained, as well as using punch through devices not in avalanche, indicated that the high energy emission spectrum is electron dominated, thus favoring indirect interband hot electron and hole (*c-v*) recombination or hot electron intraband transitions (*c-c*) as the dominant processes for the higher photon energies.

The four radiative processes relevant to our experimental devices to be considered are shown in Fig. 6, in the silicon band structure.

B. Interband Recombination

It has generally been accepted that the dominant interband radiative recombination process is the indirect, phonon assisted (PA) interband *c-v* recombination process between hot electrons in the conduction band, and holes in the valence band in equilibrium with the lattice. This should give rise to an emission spectrum ranging from about 1.1 eV (band gap of Si) to higher energies as determined by the EED function. The photon emission spectrum as a result of this process should have the general shape shown in Fig. 7(a), which is basically the EED function in Fig. 5 shifted more positive by 1.1 eV.

In Fig. 7(a) the spectral "signature" at 4 eV, due to the second maximum of the DOS function at 2.9 eV, will only be experimentally observed if there are sufficient hot electrons present at that energy level, which will only occur at high electric fields and high current densities. Furthermore, any direct interband (*c-v*) recombination in silicon should result in a fairly narrowband photon emission spectrum around 3.4 eV (the Γ - Γ direct band gap of silicon shown in Fig. 6), as depicted in Fig. 7(a).

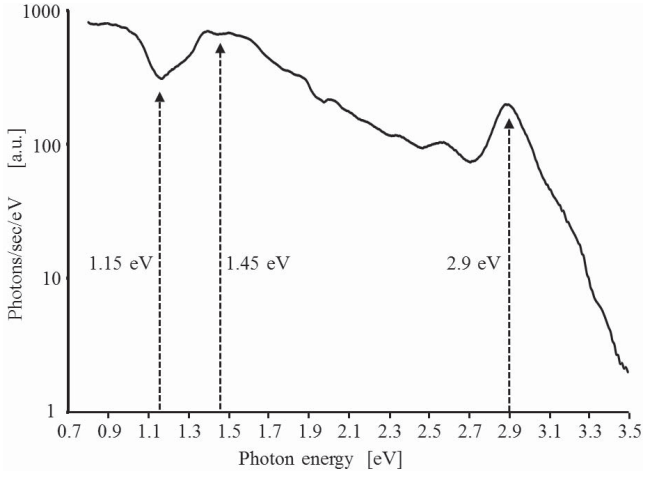

Fig. 8. The measured room temperature emission spectrum of the n^+p diode under reverse avalanche conditions and 140 mA reverse current. Two maxima are shown, a broad peak at 1.45 eV and a second narrower peak at 2.9 eV, similar in shape to the high electric field EED curves in Fig. 5. A transition region occurs at 1.15 eV.

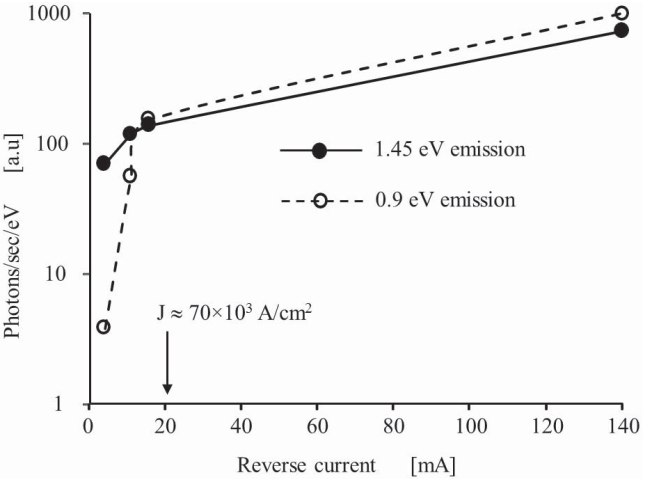

Fig. 9. The measured photon emission rates at photon energies of 0.9 eV and 1.45 eV as a function of reverse current. The low energy photon emission at 0.9 eV is very small at low currents, but above 20 mA it reaches values similar to that of the 1.45 eV emission. The 20 mA reverse current corresponds to a current density of about 70 × 103 A/cm^2.

C. Intraband Transitions

The intraband transitions can be direct or indirect, with the indirect transitions either phonon assisted (PA) or ionized impurity assisted (IA). The IA transitions are also referred to as Bremsstrahlung. Furthermore, the intraband transitions can be either that of hot electrons (*c*-*c*) or hot holes (*v*-*v*). Since our test structure is an n^+-p diode, we would expect the electron density to be substantially higher than the hole density in the high electric field region of the junction, thus the *c*-*c* transitions should dominate at higher energies.

The Bremsstrahlung origin of the hot-carrier-induced light emission was critically reviewed [19] with the eventual conclusion that Bremsstrahlung cannot be considered an acceptable quantitative description of the light generation mechanism. It was further concluded that electron energy relaxations between states of the conduction bands (*c*-*c*) are the most likely processes responsible for the hot-carrier-induced luminescence in silicon. Using an innovative double gate MOS transistor structure [23], new insight was obtained on the contribution of Bremsstrahlung to the emitted light intensity. It was concluded from this study that direct and indirect phonon assisted (PA) intraband transitions appear to be the dominant emission mechanisms in silicon.

Direct intraband transitions can only occur between conduction bands as shown in Fig. 6. As a result of this, there will be a relationship between the photon energy emitted from such direct *c*-*c* transitions and the electron energy distribution in the conduction band [24]. The direct intraband *c*-*c* transitions should exhibit an emission spectrum shown in Fig. 7(b), with a "signature" spectral peak near 2 eV. The indirect PA intraband hot electron *c*-*c* transition process should emit a spectrum following the general shape of the EED function of Fig. 7(b), also with a "signature" peak near 2.9 eV, the second maximum of the DOS function.

V. Experimental Results

In the design of the test structure (see Fig. 1) the aim was to achieve as high an electric filed as possible, without initiating field emission breakdown of the junction. Field emission breakdown will significantly reduce the internal quantum efficiency [25]. Under high electric field conditions, the spectral "signatures" that may potentially be observed as peaks in the emission spectrum for the different photon generation mechanisms are:

1) Direct interband *c*-v recombination: 3.4 eV
2) Indirect interband *c*-v recombination: 4.0 eV
3) Direct intraband *c*-*c* electron transitions: 2.0 eV
4) Indirect intraband *c*-*c* electron transitions: 2.9 eV

The photon energies of these "signatures" will be helpful in identifying the dominant light generation processes.

A typical measured room temperature photon emission spectrum at 140 mA reverse current is shown in Fig. 8. The relative flatness of the emission spectrum (at least up to 3 eV) is indicative of quite a large electric field in the device, with the 3 eV emissions only about 1 decade below the low energy peak at 1.45 eV. In comparison, previous experimental results [15], [20] showed at least two decades decrease in emission from 1.5 eV to 3 eV.

The main features observed in Fig. 8 are:

1) The broad low energy peak near 1.45 eV, which is consistent with the electron energy distribution functions as shown in Fig. 4.

2) The second high energy peak at 2.9 eV, which is a clear indication that the indirect phonon assisted intraband *c*-*c* hot electron transitions form the dominant radiative mechanism.

3) An apparent transition from one radiation mechanism to another at 1.15 eV,

4) A very sharp cut-off above 3 eV photon energy. This may also be due to the sharp cut-off of the measurement setup.

Radiometer measurements indicate that approximately 100 nW of optical power is being generated within the silicon

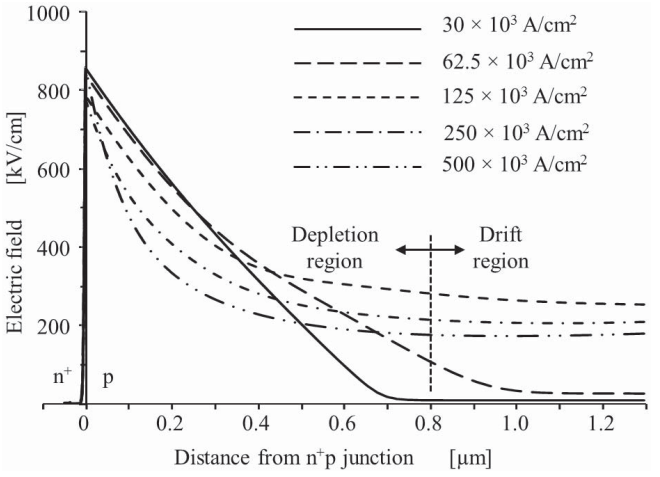

Fig. 10. The simulated distribution of the electric field in the device at different current densities as a function of distance from the n^+p metallurgical junction. The solid line is the classical triangular shaped electric field distribution at low current densities. The acceptor doping in the p-type drift region was simulated as NA = 1017 /cm^3.

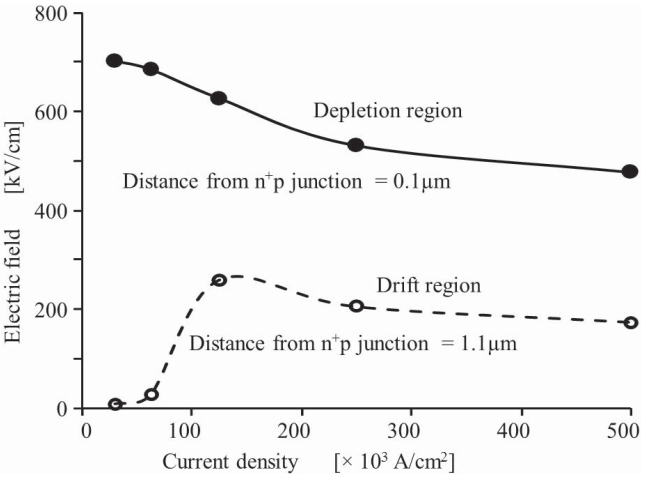

Fig. 11. The simulated electric field in the depletion and drift regions of the device. The electric field increases sharply at a current density of 100 × 103 A/cm^2 in the drift region and then remains relatively constant at 200 kV/cm. In the depletion region the high electric field condition extends to very low current levels.

bulk per 1 mA of drive current. The significant radiation at lower energies will lead to increased internal quantum efficiency. From the solid viewing angle of the radiometer, coupled with the radiation leaving the front surface and the radiation pattern of Fig. 3, the internal quantum efficiency (photons/electron) is estimated to be 0.012 %.

From Fig. 8 the conclusion may be drawn that there are two separate light generation mechanisms, one dominant at higher energies ($>$ 1.15 eV) and the other dominant at lower energies ($<$ 1.15 eV). The main mechanism responsible for the broad band photon emission with photon energies in excess of 1.15 eV has above been identified by us as being indirect intraband hot electron *c-c* transitions. The broad band low energy photon emission below 1.15 eV includes energies smaller than the band gap of silicon; it can thus be concluded that the low energy photon emission below 1.15 eV is also due to intraband carrier transitions.

The discontinuity of photon emission around 1.15 eV is thus not due to another physical mechanism, but maybe due to a device characteristic. In order to investigate the near infrared emission ($<$ 1.15 eV), the effect of reverse current on photon emission was measured. The measured photon emission rates at 0.9 eV and 1.45 eV photon energies were measured as a function of reverse current. The result is depicted in Fig. 9.

Fig. 9 indicates that below 20 mA current, the low energy photon emission is at a very low value compared to the 1.45 eV emission, but above 20 mA current the two emissions are comparable. Taking the device feature size of 350 nm and a junction depth of 200 nm into account, it is estimated that the reverse current density at the threshold current level of 20 mA is in the order of 70 $\times$ 10^3 A/cm^2 near the junction.

VI. Device Simulations

A one dimensional device simulation was performed using the Sentaurus TCAD modeling software [26] in order to get an indication of the electric field distribution and electron concentrations in the device. Although the device shown in Fig. 1 has a rather complicated three dimensional structure, we should be able to explain device behavior in terms of the one dimensional simulation results. To analyze the device behavior we employ a drift-diffusion model to describe the transport of carriers in the device. This information is obtained by solving self consistently the continuity equations for holes and electrons and Poisson's equation for the whole device, including appropriate boundary conditions at the contacts. The device operation is analyzed in the case of either a constant voltage applied to the contacts or a constant current is forced through the device.

In Fig. 10 is shown the electric field distribution in the device as a function of current density. The electric field distribution is the classical result (linear decrease of field with distance) at low current densities, but quite different field distributions are observed at higher current densities. Two regions can be defined for the device, namely 1) the high field depletion region where avalanche multiplication will take place, and 2) the drift region with fairly constant, but lower electric field. The longer the drift region, one can expect the current density to decrease towards the ohmic p^+ contact.

An interesting relationship that can be derived from Fig. 10 is the variation of electric field with current density at a constant distance from the n^+p interface. This result is shown in Fig. 11 for distances 0.1 μm (depletion region) and 1.1 μm (drift region) from the interface.

It can be seen in Fig. 11 that in the depletion region the electric field will decrease slightly with increasing current density, but on average the field will have a value approximately 600 kV/cm. In the drift region the electric field will be very low for low current densities, but at a current density value of 100 $\times$ 10^3 A/cm^2 it will increase sharply to a value of about 200 kV/cm, after which the field will remain almost constant at this value for even higher current densities. The simulated electron carrier density as a function of distance in the device is also shown in Fig. 12.

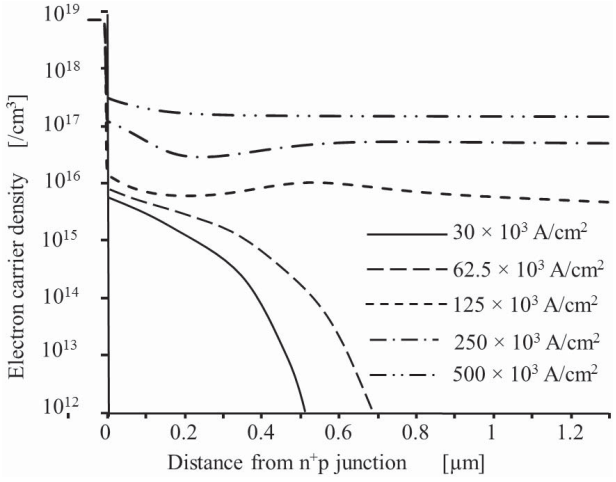

Fig. 12. The simulated electron carrier density distribution in the device at different current densities. Below 100×10^3 A/cm^2 the electron concentration in the drift region (distance from junction > 0.8 μm) is very low. This threshold current density of 100×10^3 A/cm^2 will be a function of the acceptor doping in the p-type drift region as well as of the device geometry.

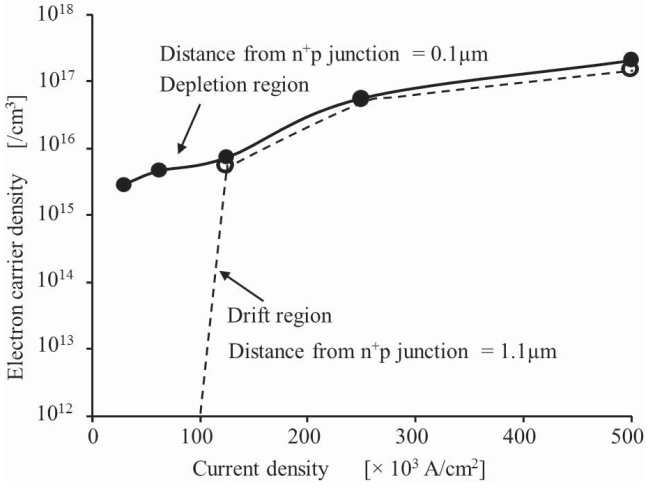

Fig. 13. The electron carrier density in the depletion and drift regions of the device at different current densities. At a current density of 100×10^3 A/cm^2 the electron concentration in the drift region falls to a very small value. The correlation between this figure and the measured photon emission shown in Fig. 9 is observed.

In Fig. 12 it is shown that in the drift region the electron carrier density is small for current densities less than 100×10^3 A/cm^2. For current densities higher than this value, the electron carrier densities are basically the same in both the depletion and drift region. Again the variation of electron density with current density at a constant distance from the n$^+$p interface can be derived. This result is shown in Fig. 13 for distances 0.1 μm (depletion region) and 1.1 μm (drift region) from the interface. From Fig. 13 it can be seen that the electron carrier density increases with increasing current density, as expected. The electron density in the drift region is very similar to that of the depletion region for current densities above 100×10^3 A/cm^2, but below this value of current density the electron density drops suddenly to a very low value.

VII. Interpretation of Results

From the measured spectrum (Fig. 8) and the photon energy "signature" of the second peak in the DOS function, we identify indirect intraband hot electron *c-c* transitions as the main light generating mechanism. This is in line with an analysis performed recently on similar devices [27].

The photon emissions from the high electric field depletion region of the device emits a spectrum (see Fig. 8) that correlates well with the 600 kV/cm electron energy distribution (see Fig. 5). Emission from the low electric field drift region only becomes noticeable above a current density of about 100×10^3 A/cm^2 when the electric field increases rapidly to a value of about 200 kV/cm (see Figs. 9, 11, and 13), where it remains for larger current densities. This photon emission from the drift region is also due to indirect intraband hot electron *c-c* transitions, since the low photon energy drift region emission spectrum correlates very well with the 200 kV/cm electron energy distribution (see Fig. 5). It then follows that the photon emission spectra of Fig. 8 at high current density constitutes the combined effect of the 200 kV/cm and 600 kV/cm electron energy distributions shown in Fig. 5. At low current densities in the drift region, only the 600 kV/cm spectrum from the depletion region will be observed. It can thus be concluded that the two spectra (< 1.15 eV and > 1.15 eV) observed in Fig. 8 emanate from two different regions in the device, namely the high electric field depletion region (> 1.15 eV) and the low electric field drift region (< 1.15 eV). Since the drift region geometry and doping levels will be a strong function of the device design and process technology, the threshold level of reverse current to initiate low photon energy emissions from the drift region may vary significantly from our observed 70-100 $\times 10^3$ A/cm^2.

Acknowledgment

The authors would like to thank Christo Janse van Rensburg and Alfons Bogalecki (INSiAVA (Pty) Ltd., Pretoria, South Africa) for performing the measurements. We also would like to thank Hanqing Wen (Boston University, Boston MA, USA) for the device simulations.

References

[1] N .R. Savage, "Holy grail: Light from silicon," in *Proc. IEEE Spectr. Conf.*, Jan. 2004, pp. 51–59.

[2] L. Pavesi, S. Gaponenko, and L. Dal Negro, *Nato Science Series II: Mathematics, Physics and Chemistry Series*, vol. 93, Boston, MA, USA: Kluwer Academic Publishers, 2003.

[3] D. Liang and J. E. Bowers, "Recent progress in lasers on silicon," *Nature Photon.*, vol. 4, no. 8, pp. 511–517, 2010.

[4] C. Ciminelli, P. Frascella, and M. N. Armenise, "Optical modelling of a Si-based DBR laser source using a nanocrystal Si-sensitized Er-doped silica rib waveguide in the C-band," *J. Eur. Opt. Soc. Rapid Publications*, vol. 3, pp. 08017-1–08017-6, Jan. 2008.

[5] N. Izhaky, M. T. Morse, S. Koehl, O. Cohen, D. Rubin, A. Barkai, G. Sarid, R. Cohen, and M. J. Paniccia, "Development of CMOS-compatible integrated silicon photonic devices," *IEEE J. Sel. Topics Quantum Electron.*, vol. 12, no. 6, pp. 1688–1698, Nov.–Dec. 2006.

[6] M. du Plessis, H. Aharoni, and L. W. Snyman, "Silicon LEDs fabricated in standard VLSI technology as components for all silicon monolithic integrated optoelectronic systems," *IEEE J. Sel. Topics Quantum Electron.*, vol. 8, no. 6, pp. 1412–1419, Nov.–Dec. 2002.

[7] P. J. Venter, M. du Plessis, A. W. Bogalecki, M. E. Goosen, and P. Rademeyer, "An 8 × 64 pixel dot matrix microdisplay in 0.35 micron CMOS technology," *Opt. Eng.*, vol. 51, no. 1, p. 014003, 2012.

[8] A. R. Chen, A. I. Akinwande, and H.-S. Lee, "CMOS-based microdisplay with calibrated backplane," *IEEE J. Solid-State Circuits*, vol. 40, no. 12, pp. 2746–2755, Dec. 2005.
[9] A. Chatterjee, P. Mongkolkachit, B. Bhuva, and A. Verma, "All Si-based optical interconnect for interchip signal transmission," *IEEE Phot. Tech. Lett.*, vol. 15, no. 11, pp. 1663–1665, Nov. 2003.
[10] S. Sayil, "Avalanche breakdown in silicon devices for contactless logic testing and optical interconnect," *Analog Integr. Circuit Signal Process.*, vol. 56, no. 3, pp. 213–221, 2008.
[11] L. Rebohle, T. Gebel, R. A. Yankov, T. Trautmann, W. Skorupa, J. Sun, G. Gauglitz, and R. Frank, "Microarrays of silicon-based light emitters for novel biosensor and lab-on-a-chip applications," *Opt. Mater.*, vol. 27, no. 5, pp. 1055–1058, 2005.
[12] K. Misiakos, P. S. Petrou, S. E. Kakabakos, M. E. Vlahopoulou, A. Tserepi, E. Gogolides, and H. H. Ruf, "Monolithic silicon optoelectronic transducers and elastomeric fluidic modules for bio-spotting and bio-assay experiments," *Microelectron. Eng.*, vol. 83, nos. 4–9, pp. 1605–1608, 2006.
[13] R. Newman, W. C. Dash, R. N. Hall, and W. E. Burch, "Visible light from a Si p-n junction," *Phys. Rev.*, vol. 98, no. 1, pp. 1536–1537, 1955.
[14] L. Tirino, M. Weber, K. F. Brennan, and E. Bellotti, "A general Monte Carlo model including the effect of the acoustic deformation potential on the transport properties," *J. Comput. Electron.*, vol. 3, no. 2, pp. 81–93, 2005.
[15] M. V. Fischetti, "Monte Carlo simulation of transport in technologically significant semiconductors of the diamond and zinc-blende structures-Part I: Homogeneous transport," *IEEE Trans. Electron Devices*, vol. 38, no. 3, pp. 634–649, Mar. 1991.
[16] R. Brunetti, C. Jacoboni, F. Venturi, E. Sangiorgi, and B. Riccò, "A many-band silicon model for hot-electron transport at high energies," *Solid-State Electron.*, vol. 32, no. 12, pp. 1663–1667, 1989.
[17] T. Mietzner, J. Jakumeit, and U. Ravaioli, "Local iterative Monte Carlo analysis of electron-electron interaction in short-channel Si-MOSFETs," *IEEE Trans. Electron Devices*, vol. 48, no. 10, pp. 2323–2330, Oct. 2001.
[18] A. G. Chynoweth and K. G. McKay, "Photon emission from avalanche breakdown in silicon," *Phys. Rev.*, vol. 102, no. 2, pp. 369–376, 1956.
[19] A. L. Lacaita, F. Zappa, S. Bigliardi, and M. Manfredi, "On the Bremsstrahlung origin of hot-carrier-induced photons in silicon devices," *IEEE Trans. Electron Devices*, vol. 40, no. 3, pp. 577–582, Mar. 1993.
[20] N. Akil, S. E. Kerns, D. V. Kerns, A. Hoffmann, and J.-P. Charles, "A multimechanism model for photon generation by silicon junctions in avalanche breakdown," *IEEE Trans. Electron Devices*, vol. 46, no. 5, pp. 1022–1028, May 1999.
[21] A. G. Chynoweth and H. K. Gummel, "Photon emission from avalanche breakdown in germanium p-n junctions," *J. Phys. Chem. Solids*, vol. 16, nos. 3–4, pp. 191–197, 1960.
[22] G. Deboy and J. Kölzer, "Fundamentals of light emission from silicon devices," *Semicond. Sci. Technol.*, vol. 9, no. 5, pp. 1017–1032, 1993.
[23] L. Selmi, H. S. Wong, M. Lanzoni, E. Sangiorgi, and M. Manfredi, "Investigation of hot electron luminescence in silicon by means of dual gate MOS structures," in *Proc. IEDM Tech. Dig.*, 1993, pp. 531–534.
[24] N. Asli, M. I. Vexler, A. F. Shulekin, P. D. Yoder, I. V. Grekhov, and P. Seegebrecht, "Threshold energies in the light emission characteristics of silicon MOS tunnel diodes," *Microelectron. Rel.*, vol. 41, no. 7, pp. 1071–1076, 2001.
[25] M. du Plessis and P. Rademeyer, "Novel electroluminescence technique to analyze mixed reverse breakdown phenomena in silicon diodes," *Solid State Electron.*, vol. 54, no. 4, pp. 433–438, 2010.
[26] (Jun. 2012). *Sentaurus Device User Guide* [Online]. Available: www.synopsys.com
[27] H. Elghazi, A. Jorio, and I. Zorkani, "Analysis of silicon light emission under breakdown condition using an indirect intraband model," *Opt. Commun.*, vol. 281, no. 12, pp. 3320–3323, 2008.

Monuko du Plessis (M'76–SM'81) was born in King Williamstown, South Africa, in 1949. He received the B.Eng., M.Eng., and the D.Eng. degrees in electrical engineering from the University of Pretoria, Pretoria, South Africa, in 1972, 1978 and 1984, respectively, and the B.A. degree in psychology and B.Com. (Hons) degree in economics from the University of South Africa, Pretoria 0002, South Africa, in 1989 and 1998, respectively.

He joined the Department of Electrical Engineering, University of Pretoria, as Research Officer in microelectronics and optoelectronics. He was the Director of the Carl and Emily Fuchs Institute for Microelectronics (CEFIM), University of Pretoria from 1991 to 2012, and is currently a Full Professor with the Department of Electrical, Electronic and Computer Engineering, University of Pretoria. His current research interests include silicon photonics and analog CMOS integrated circuit design.

Prof. Plessis is a member of SPIE and a Registered Professional Engineer with the Engineering Council of South Africa (ECSA). He is also an IEEE ED Society Distinguished Lecturer in Region 8.

Petrus J. Venter (M'04–SM'13) received the B.Eng. degree in electronic engineering in 2004 and the M.Eng. degree in 2009 from the University of Pretoria, Pretoria, South Africa. He is currently pursuing the Ph.D. degree in silicon light emission.

He was an Assistant Lecturer with the University of Pretoria from 2005 to 2006. In 2007, he was a Lecturer and started to practice engineering in a start-up company called INSiAVA founded in the same year. He is currently an Senior Lecturer Research Engineer with the University of Pretoria.

Mr. Venter was a recipient of the SAMES Award for Best Microelectronic Student in 2004 and a first prize in the Design Automation Conference's student paper contest in 2005. In 2006, he was awarded the Tanner Award for Outstanding Achievement in Educational Design.

Enrico Bellotti (A'11) received the "Laurea in Ingegneria Electtronica" degree from Politecnico di Milano, Milano, Italy, in 1989, and the Ph.D. degree in electrical engineering from the Georgia Institute of Technology, Atlanta, GA, USA, in 1999. He has been with the Electrical and Computer Engineering Department, Boston University, Boston, MA, USA, since September 2000, initially as an Assistant Professor from 2000 to 2006 then with the rank of Associate Professor from 2006 to 2012), and a Professor since 2013.

He has over 20 years of experience in electronic and optoelectronic device simulation, and computational electronics research. He has authored over 75 journal papers, 60 conference papers, and 4 book chapters. He hods two U.S. patents. He has done research on InGaAs/InP and AlGaN/GaN HEMTs design, GaN-based permeable base transistors, near-infrared detectors, avalanche photodiodes, high-field transport study in wide band-gap semiconductors, UV optoelectronics devices, and multispectral IR detectors. His current research interests include the microscopic simulation of terahertz emitters, avalanche and single-photon detectors, oxide semiconductor materials, and electromagnetic simulation of 3-D synthetic structures intended for emitter/detector performance enhancement.

Dr. Bellotti was a recipient of the 2003 ONR Young Investigator Program Award and the 2005 NSF CAREER Award.